UC Berkeley

UC Berkeley Previously Published Works

Title

Unlocking Li superionic conductivity in face-centred cubic oxides via face-sharing configurations

Permalink

https://escholarship.org/uc/item/79n3d2g6

Journal

Nature Materials, 23(4)

ISSN

1476-1122

Authors

Chen, Yu

Lun, Zhengyan

Zhao, Xinye

et al.

Publication Date

2024-04-01

DOI

10.1038/s41563-024-01800-8

Copyright Information

This work is made available under the terms of a Creative Commons Attribution-NonCommercial License, available at https://creativecommons.org/licenses/by-nc/4.0/

Peer reviewed

eScholarship.org Powered by the California Digital Library
University of California

Unlocking Li superionic conductivity in face-centered cubic oxides via face-sharing configurations

Yu Chen[1,2], Zhengyan Lun[3,4], Xinye Zhao[1,2], Krishna Prasad Koirala[5], Linze Li[6], Yingzhi Sun[1,2], Christopher A. O'Keefe[3], Xiaochen Yang[1,2], Zijian Cai[1,2], Chongmin Wang[6], Huiwen Ji[7,*], Clare P. Grey[3,*], Bin Ouyang[8,*], Gerbrand Ceder[1,2,*]

[1] Department of Materials Science and Engineering, University of California, Berkeley, Berkeley, CA, USA

[2] Materials Sciences Division, Lawrence Berkeley National Laboratory, Berkeley, CA, USA

[3] Yusuf Hamied Department of Chemistry, University of Cambridge; Cambridge, UK

[4] School of Chemical Sciences, University of Chinese Academy of Sciences, Beijing, China

[5] Physical and Computational Sciences Directorate, Pacific Northwest National Laboratory, Richland, WA, USA

[6] Environmental Molecular Sciences Laboratory, Pacific Northwest National Laboratory, Richland, WA, USA

[7] Department of Materials Science and Engineering, University of Utah, Salt Lake City, UT, USA

[8] Department of Chemistry and Biochemistry, Florida State University, Tallahassee, FL, USA

* Corresponding authors:

Prof. Huiwen Ji (Email: huiwen.ji@utah.edu)

Prof. Clare P. Grey (Email: cpg27@cam.ac.uk)

Prof. Bin Ouyang (Email: bouyang@fsu.edu)

Prof. Gerbrand Ceder (Email: gceder@berkeley.edu)

Abstract

Oxides with a face-centered cubic (*fcc*) anion sublattice are generally not considered as solid-state electrolytes as the structural framework is thought to be unfavorable for Li superionic conduction. Herein, we demonstrate Li superionic conductivity in *fcc*-type oxides in which face-sharing Li configurations have been created through cation over-stoichiometry in rocksalt-type lattices via excess Li. We find that the face-sharing Li configurations create a novel spinel with unconventional stoichiometry and raise the energy of Li, thereby promoting fast Li-ion conduction. The over-stoichiometric Li–In–Sn–O compound exhibits a total Li superionic conductivity of 3.38×10^{-4} S cm^{-1} at room temperature with a low migration barrier of 255 meV. Our work unlocks the potential of designing Li superionic conductors in a prototypical structural framework with vast chemical flexibility, providing a fertile ground for discovering new solid-state electrolytes.

The tremendous interest in all-solid-state batteries (ASSBs), driven by their enhanced safety and potential compatibility with a lithium (Li)-metal anode, has brought solid-state superionic conductors (SICs) to the forefront of battery research[1,2]. SICs with high ionic conductivities as well as excellent chemical and electrochemical stability are the key to realizing practical ASSBs[3,4]. To date, multiple sulfide-based SICs, including $Li_{10}GeP_2S_{12}$[5], $Li_{9.54}Si_{1.74}P_{1.44}S_{11.7}Cl_{0.3}$[6], and lithium argyrodites[7], have been discovered to have high Li-ion conductivity, exceeding that of conventional liquid electrolytes (~10 mS cm^{-1}). However, the narrow electrochemical stability window, poor chemical stability, and high moisture sensitivity of sulfides have limited their application in ASSBs[8-11]. Oxide-based SICs tend to have better air and electrochemical stability, but at the cost of lower ionic conductivity[3,12]. Thus far, room-temperature (RT) Li ion conductivity > 0.1 mS cm^{-1} has been reported only in a handful of oxides (e.g., Li garnets[13,14], NASICON-type Li oxides[15], and Li perovskites[16]), all of which have uncommon oxygen packing. Surprisingly, the most common class of oxides, those with a close-packed face-centered cubic (*fcc*) anion sublattice, have so far not displayed high enough Li-ion mobility to be considered as SICs. The traditional rationale for excluding *fcc*-type oxides from the search for potential SICs is that the activation energy for Li motion is expected to be high, because the Li-ion migration path must cross through both tetrahedral (Tet) and octahedral (Oct) sites with very different site energies[17], as shown in Fig. 1a.

As a strategy to enhance the Li-ion conductivity in *fcc*-type oxides, we propose to construct a face-sharing Li configuration, in which Li ions simultaneously occupy the neighboring sites that are face-sharing. As shown in Fig. 1b, such a face-sharing configuration raises the energy of Li ion and thus flattens the energy landscape for ion migration. Furthermore, the strong Li–Li interactions between face-sharing sites can activate concerted ion migration, as reported for many

SICs[18,19]. The formation of distorted face-sharing Li–O polyhedra has also emerged as a key mechanism to account for the fast kinetics observed in several Li-ion anodes (e.g., $Li_4Ti_5O_{12}$[20], $Li_3V_2O_5$[21]).

In this work, we demonstrate that we can create face-sharing configurations in *fcc*-type oxides by incorporating excess Li to yield cation over-stoichiometry (Li over-stoichiometry for short) in a Li–In–Sn–O compound (o-LISO). The resulting material exhibits a Li-ion conductivity of 3.38×10^{-4} S cm^{-1} at RT with a remarkably low migration barrier of 255 meV, significantly superior to rocksalts that contain a stoichiometric amount of cations. Furthermore, we observe a surprising spinel-like ordering of the cations even though the cation/anion ratio is > 1 in this compound. This phenomenon leads to a unique nanosized phase (s-phase) with improved three-dimensional (3D) percolation of face-sharing Li and enhanced ionic conductivity compared with that of the cation-disordered state. This success motivated us to further investigate the thermodynamic stability of over-stoichiometric rocksalt-type oxides composed of many other metal species, with the aim of providing guidelines to accelerate future SIC exploration within this vast new design space.

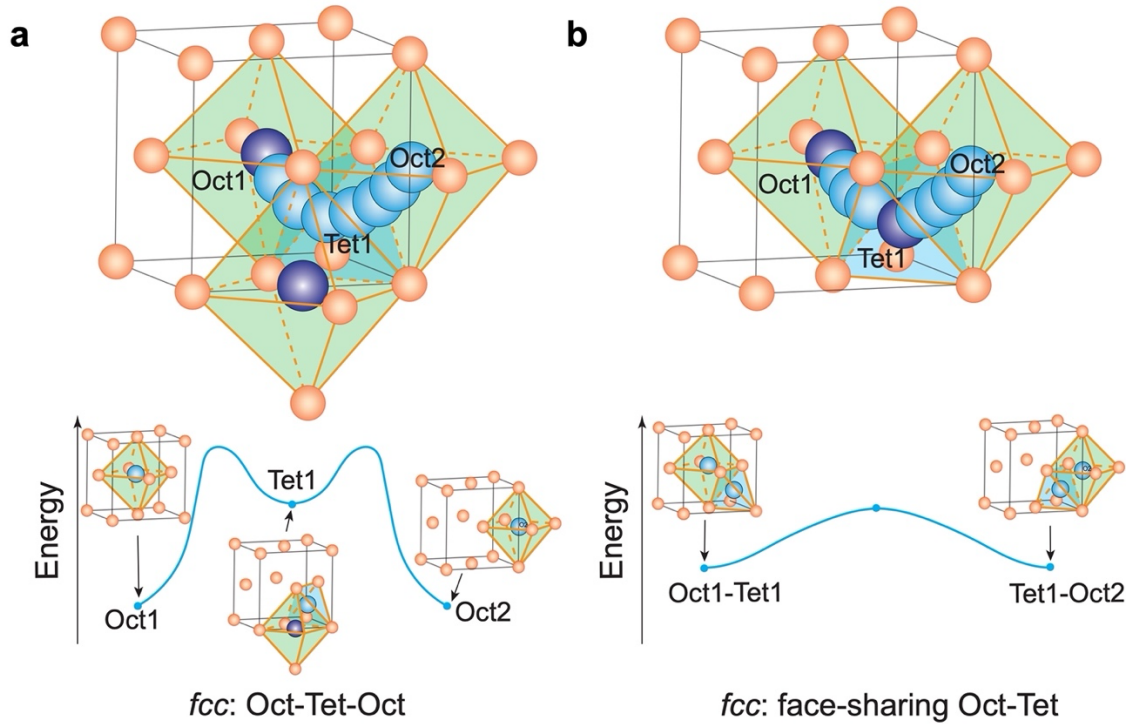

Figure 1. Schematic illustration of Li-ion migration pathways in *fcc*-type oxides. (a) Oct-Tet-Oct pathway in *fcc* oxygen lattice without face-sharing Li in the initial state (upper panel) and the energy landscape (lower panel). **(b)** Oct-Tet/Tet-Oct pathways in *fcc* oxygen lattice with face-sharing Li in the initial state (upper panel) and the energy landscape (lower panel). The oxygen anions are colored orange, and the Li ions are colored purple for initial sites and blue for migration paths.

Li superionic conductivity in o-LISO

Stoichiometric rocksalt-type oxides feature a cation to anion ratio of 1. To create a face-sharing Li configuration, we introduce excess Li to form an over-stoichiometric rocksalt-type (ORX) oxide. As an example, $Li_{17}In_9SnO_{24}$ (o-LISO), was synthesized by using a conventional solid-state method. The synchrotron X-ray diffraction (XRD) pattern of o-LISO (Supplementary Fig. 1) shows sharp peaks of a rocksalt lattice along with additional broad peaks which together can be

indexed to the *Fd-3m* space group. Detailed structure analysis is presented in the subsequent sections.

The Li-ion conductivity of o-LISO was measured using electrochemical impedance spectroscopy (EIS). As shown in Figs. 2a–b, the Nyquist plots consist of a semicircle at high frequency and a linear tail at low frequency, characteristic of purely ionic conductors. The equivalent circuit fitted total ionic conductivity of o-LISO, including both the bulk and grain-boundary contributions, is 3.38×10^{-4} S cm^{-1} at RT (Supplementary Fig. 2 and Note 1). The activation energy of Li-ion conduction in o-LISO is estimated to be 255 meV from a linear fit to the Arrhenius plot (Fig. 2b). A d.c. polarization experiment gives a RT electronic conductivity of 2.47×10^{-9} S cm^{-1} (Supplementary Fig. 3), five orders of magnitude lower than the ionic conductivity. This performance of o-LISO is comparable to that of current state-of-the-art oxide-based SICs (e.g., garnet-type $Li_7La_3Zr_2O_{12}$[14] and NASICON-type $Li_{1.3}Al_{0.3}Ti_{1.7}(PO_4)_3$[15]) and is significantly superior to that of typical *fcc*-type Li-M-oxides reported in the literature, e.g., Li_2MgTiO_4 (~9×10^{-5} S cm^{-1} at 600 °C, E_a = 0.53 eV)[22], $Li_{2.8}Ni_{0.1}NbO_4$ (~5×10^{-4} S cm^{-1} at 300 °C, E_a ~ 0.6 eV)[23], and $Li_4Ti_5O_{12}$ (~7×10^{-8} S cm^{-1} at RT, E_a ~ 0.5 eV)[24]. Notably, the activation energy is lower than that of most oxide SICs (Supplementary Fig. 4), indicating that facile Li-ion conduction is achieved in this ORX compound.

The Li-ion dynamics in o-LISO were further probed using variable-temperature ^{6}Li solid-state NMR (ssNMR) from 226 K to 386 K. The spectra in Fig. 2c can be fit with two Li sites, which are assigned to Tet (site 1, higher chemical shift) and Oct (site 2, lower chemical shift) coordination environments, respectively[25]. With increasing temperature, a narrowing of the peak width for both sites is observed, but is much more pronounced for site 1, dropping from more than 10 ppm to less than 7 ppm full width at half height (FWHH). The narrowing (coupled with the extremely short

relaxation times, Supplementary Table 1) suggests enhanced Li mobility involving this site. In addition, the integrated intensity ratio between site 1 and site 2 increases as the temperature rises from approximately 1:4 at 226 K approaching 1:1 at 386 K (Supplementary Table 1), which implies thermal population of a higher energy site at higher temperatures, presumably enabled by Li hopping. The local Li-hopping barriers are 57 meV for site 1 and 74 meV for site 2 from fitting the Arrhenius plot of the ^{6}Li spin-lattice relaxation rate with respect to inverse temperature (Fig. 2d). These values are much smaller than the apparent activation energy determined from EIS (i.e., 255 meV) because EIS measures the overall macroscopic Li-ion conductivity including the contributions from temperature-dependent correlated motion, grain boundaries and pores, whereas NMR probes the rate of local ion hopping[26]. The NMR-probed Li-hopping barriers of o-LISO are much smaller than those of other SICs reported in the literature[27-29], suggesting a very high intrinsic Li mobility in the structure.

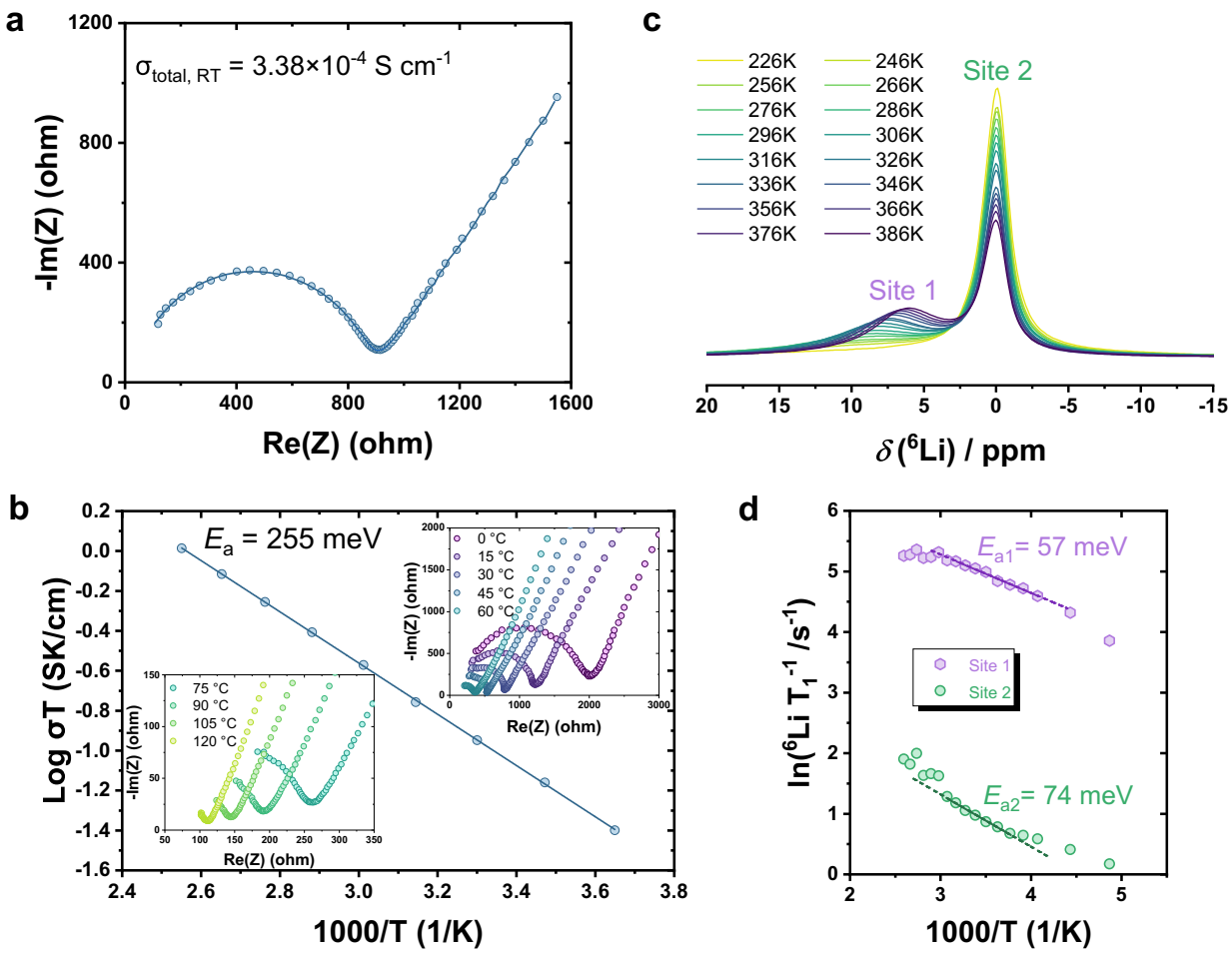

Figure 2. Li-ion conductivity of o-LISO. (a) Nyquist plot from EIS measurement at RT and the corresponding fit to the equivalent circuit. **(b)** Nyquist plots in the temperature range from 0 °C to 120 °C and Arrhenius plots of the total ionic conductivity. **(c)** ^{6}Li MAS ssNMR spectra of o-LISO at temperatures from 226 K to 386 K. **(d)** Temperature dependence of the ^{6}Li ssNMR spin-lattice relaxation rates of the two Li sites in o-LISO.

Effect of over-stoichiometric Li on phase formation

To understand the observed Li superionic conductivity in o-LISO, we investigated the phase evolution as function of the amount of over-stoichiometry. Fig. 3a presents the XRD patterns of the LISO samples prepared using the same precursors targeting the composition $Li_{17}In_9SnO_{24}$ but with different calcination times. When calcinated at 1050 °C for 4 h, three phases can be identified in the XRD pattern: cation-disordered rocksalt (DRX), an unknown phase with spinel-like reflections (denoted as the "s-phase"), and a Li_3InO_3-like phase[30] (see Supplementary Fig. 5 and Note 2 for details of the structure analysis). With longer calcination time, the Li_3InO_3-like phase first disappears, followed by the s-phase, leaving a pure DRX phase after calcinating for 10 h. Further extending the calcination time to 20 h eventually results in a sole $LiInO_2$-type phase present. Thermal gravimetric analysis shows continuous mass loss in the material when held at 1050 °C (Supplementary Fig. 6), which must arise from Li_2O loss given its volatile nature and the highly Li-rich starting composition. We thus speculate that the observed phase evolution is driven by a decreasing Li content with prolonged annealing. To confirm this speculation, a series of compositions $Li_nIn_9SnO_{(31+n)/2}$ (LISOn, n = 9, 13, 15, 17, 19) with the same In/Sn ratio but various Li contents were calcinated at 1050 °C for 4 h. The resulting XRD patterns are shown in Fig. 3b. With increasing Li content, the phases formed change from $LiInO_2$-type, to DRX, to a mixed DRX and s-phase, and finally a mixture with Li_3InO_3-like phase. This trend, summarized in Fig. 3c, is consistent with the phases observed in Fig. 3a, if indeed the Li content decreases with increasing calcination time.

Furthermore, even though both o-LISO and near-stoichiometric LISO (ns-LISO, synthesized by longer calcination time, see Methods for more details) contain a DRX phase, the diffraction peaks of the former appear at lower 2θ than for the latter (Supplementary Fig. 7). Such lattice expansion

of the DRX phase in o-LISO likely stems from the additional Li incorporated into Tet sites. We therefore differentiate the DRX phase in o-LISO by denoting it as "o-DRX". In addition, we observe the formation of a unique s-phase along with o-DRX in o-LISO, which is rather counterintuitive because oxide spinels typically form for cation-deficient compositions. The structure of this s-phase will be discussed in the next section.

Elemental analysis performed by inductively coupled plasma optical emission spectroscopy (ICP-OES) confirmed that the Li content in o-LISO (Li: In: Sn = 14.9: 9.0: 1) is indeed over-stoichiometric and much higher than that in ns-LISO (Li: In: Sn = 12.7: 9.1: 1) (Supplementary Table 2). The lower Li content in o-LISO than that in the initial composition (Li: In: Sn = 17: 9: 1) confirms Li-loss during heat treatment. In addition, compared with the Li superionic conductivity observed in o-LISO, the RT ionic conductivity in ns-LISO is four orders of magnitude lower, at 3.32×10^{-8} S cm^{-1}, and the activation energy is much higher, at 552 meV (Supplementary Fig. 8). The ionic conductivity of ns-LISO drops if the calcination time is even further increased, although the DRX phase remains throughout (see Supplementary Note 3).

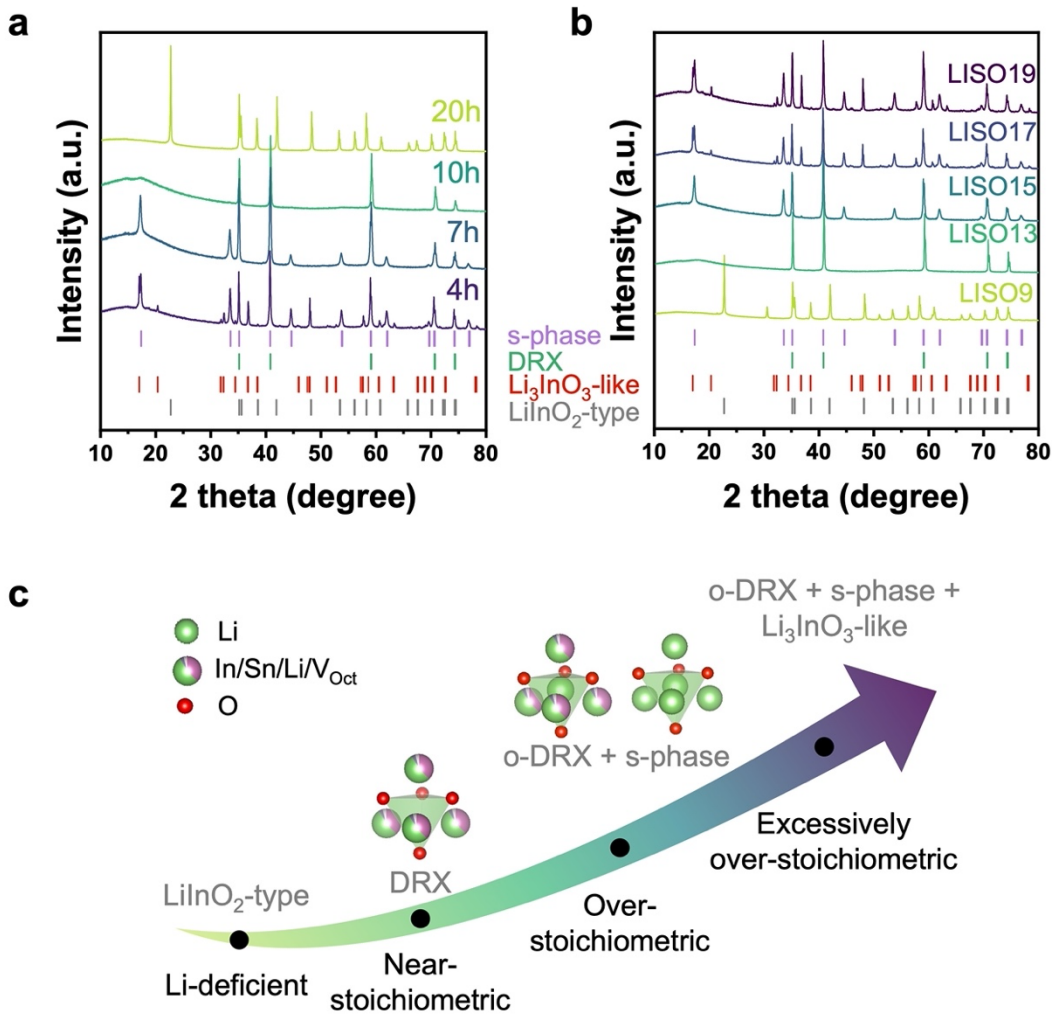

Figure 3. LISO phase evolution with varying Li content and calcination time. (a) XRD patterns of LISO samples calcined at 1050 °C for 4, 7, 10, and 20 h to achieve an increasing degree of Li evaporation. All start from the same nominal composition of $Li_{17}In_9SnO_{24}$. The Bragg positions of the phases identified are labelled by vertical tick marks: purple–s-phase, green–DRX, red–Li_3InO_3-like phase, grey–$LiInO_2$-type phase. **(b)** XRD patterns of $Li_nIn_9SnO_{(31+n)/2}$ (LISOn, n = 9, 13, 15, 17, 19) calcined at 1050 °C for 4 h. The vertical tick marks are the same as those in (a). **(c)** Schematic of phase evolution with increasing Li content in the LISO system. o-DRX refers to the DRX phase with over-stoichiometric Li content.

Evidence of face-sharing Li configurations in o-LISO

The local Li environment in o-LISO and ns-LISO was probed using ^{6}Li ssNMR, with the results shown in Fig. 4a. The ssNMR spectrum of ns-LISO shows a single peak at ~ 0 ppm reflecting the Oct-Li environment. In contrast, the ssNMR spectrum of o-LISO shows an additional peak at ~ 6 ppm, which can be attributed to Li in Tet sites. Thus, Li ions in o-LISO occupy both Oct and Tet sites, whereas ns-LISO only has Oct-Li present.

To resolve the detailed structures of the o-DRX and s-phase in o-LISO, Rietveld refinement of time-of-flight neutron powder diffraction (TOF-NPD) was performed using a two-phase model and a high-throughput grid-search method. As explained in Supplementary Fig. 9 and Note 4, the fit with a two-phase model leads to better results than the single-phase model with selective peak broadening, and is consistent with the dark-field imaging shown in later section. The refinement results are shown in Fig. 4b and Supplementary Fig. 10, and detailed methodology of the refinement is described in Supplementary Fig. 11 and Note 5. The resulting structural parameters are given in Supplementary Table 3. Visualization of the structures in Figs. 4c−d shows Li ions occupying the face-sharing Tet and Oct sites in both phases. For o-DRX, Li ions in Tet site (8c) with an occupancy of 0.058 face-share with the Oct site (4a) occupied by either Li, In, or Sn. This Tet-Li occupancy is probably the origin of the lattice expansion in o-DRX (Supplementary Fig. 7), as reported when the disordered rocksalt anode $Li_{3+x}V_2O_5$ is lithiated[21]. Unlike a typical oxide spinel which has a fully occupied 8a (Tet) site and a completely vacant 16c (Oct) site, the 16c site in the s-phase is fully occupied by Li and the 8a site is partially occupied by Li with an occupancy of 0.4. Thus, in the s-phase, Li simultaneously occupies the face-sharing 8a and 16c sites, which creates a 3D connected network (Fig. 4d). The identification of Tet−Oct face-sharing Li polyhedra

in both phases is consistent with the detection of both Oct- and Tet-Li environments in o-LISO by ssNMR (Fig. 4a).

The data in Fig. 3 indicates that the formation of the s-phase is induced by the over-stoichiometric Li. Within a rocksalt-type framework, over-stoichiometric Li must introduce some degree of Tet−Oct face-sharing occupancy among cations. We hypothesize that the energy of Tet-Li is lower if they face-share only with Li instead of with high-valent In or Sn. This contribution to the energetics will steer the ordering of metal cations away from the cation-disordered state. The cation ordering in the s-phase guarantees that face sharing only occurs among Li occupying 8a and 16c sites, similar to a regular spinel in which the 16c/16d ordering provides the 8a sites with no face-sharing cations. The appearance of the s-phase in o-LISO is thus proposed to be driven by the stabilization of face-sharing Tet-Li.

The broad superstructure peaks from the s-phase in XRD patterns (Figs. 3a−b and Supplementary Fig. 1) indicate a small domain size for the cation ordering, which is refined to be 24.5(5) nm (Supplementary Fig. 1). This domain size is much smaller than that of the co-existing o-DRX, of which the XRD peaks are sharper and only show instrumental broadening. To understand the distribution of each phase in o-LISO, the microstructure was examined using transmission electron microscopy (TEM). Fig. 4e presents the TEM electron diffraction (ED) patterns collected on o-LISO particles. Compared with the ED patterns of ns-LISO with a pure DRX phase (Supplementary Fig. 13), o-LISO shows additional Bragg diffraction spots which indicate unit-cell doubling, consistent with the spinel-like s-phase. Dark-field diffraction contrast imaging was further performed, as shown in Fig. 4f and Supplementary Fig. 14. In this dark-field mode, the s-phase regions appear bright, whereas the o-DRX regions remain dark. The images clearly show that nano-sized s-phase domains are dispersed in the o-DRX matrix within the same

crystalline particle. The domain size is a few tens of nanometers, consistent with the determination from the synchrotron XRD refinement.

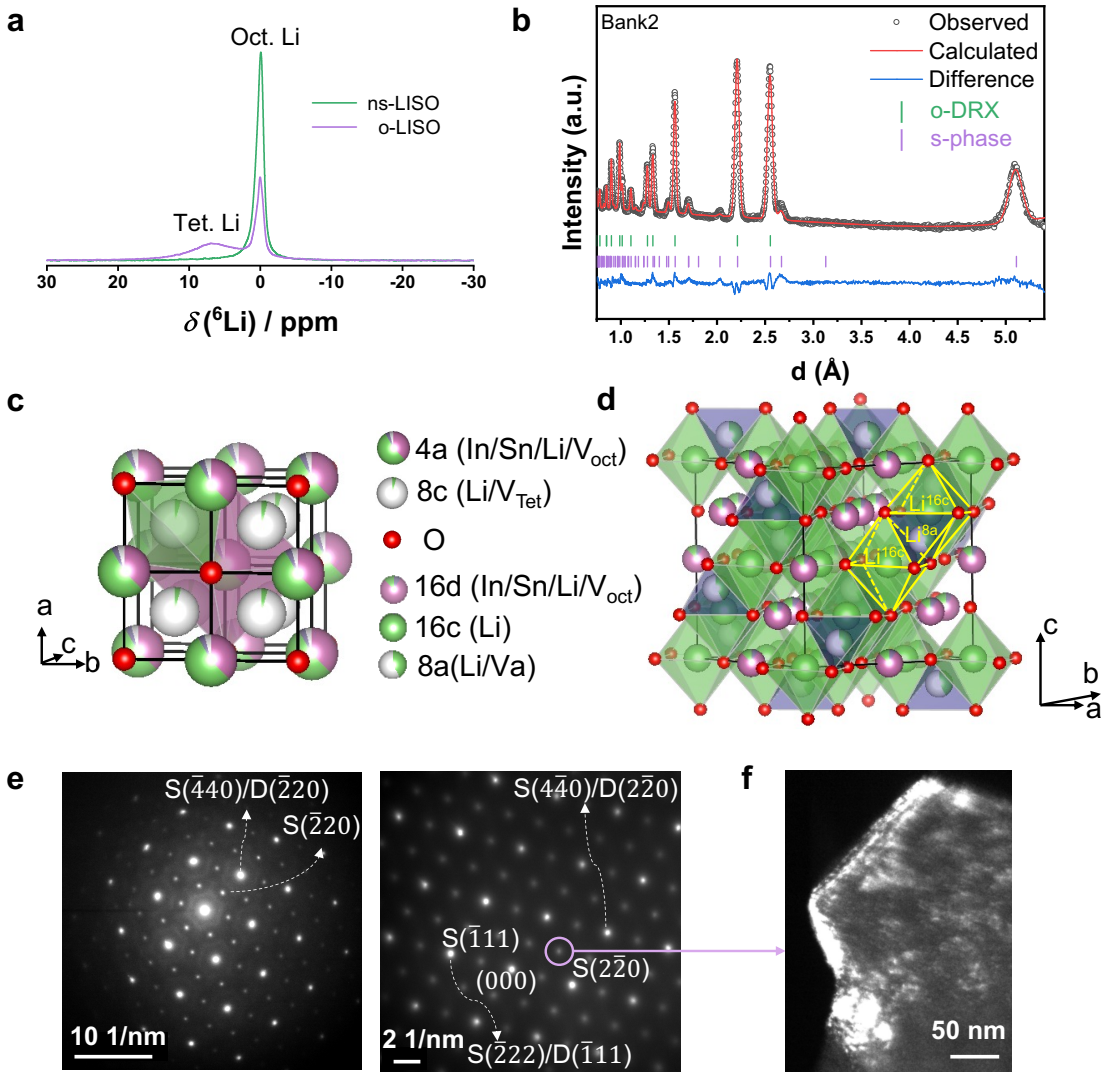

Figure 4. Structural characterization of o-LISO. (a) ^{6}Li MAS ssNMR spectra of o-LISO and ns-LISO at RT and a MAS frequency of 50 kHz. The spectra were scaled according to the amount of powder packed in the rotor and the number of scans. **(b)** TOF-NPD pattern (Bank 2) of o-LISO and Rietveld refinement. Bragg positions of o-DRX and the s-phase are marked by green and purple vertical tick marks, respectively. **(c)** Structure of o-DRX. **(d)** Structure of the s-phase. **(e)** TEM electron diffraction patterns collected on o-LISO particles along the zone axes of [111] (left)

and [110] (right). Reflections marked with "S" are indexed to the s-phase, and those marked with "D" are indexed to o-DRX. **(f)** Dark-field diffraction contrast imaging of an o-LISO particle. Only the electron beams scattered by s-phase (220) lattice planes (marked by a purple circle in (e)) were selected.

Verified fast Li^+ diffusion with face-sharing configurations

To more quantitatively connect the face-sharing Li configurations we identified in o-LISO to its high ionic conductivity, ab initio molecular dynamics (AIMD) simulations were performed on the o-DRX and s-phase. Details are provided in the Methods. The resulting Li-ion diffusivity for each phase is shown in Fig. 5a as function of temperature. Because diffusivity contains the effect of correlation and percolation, we plot in Fig. 5b the number of hops which more directly indicates the frequency of local hopping between Tet and Oct sites. The activation energy for Li-ion diffusion in o-DRX is 430 meV and 261 meV in the s-phase, with extrapolated Li-ion conductivities at 300 K of 1.22×10^{-4} S cm^{-1} for o-DRX and 3.17×10^{-3} S cm^{-1} for the s-phase. The local hopping barrier (Fig. 5b) is only 69 meV for the s-phase, which is considerably lower than the diffusion activation energy due to the different length and time scale of the ion transport probed. These calculated diffusion and local hopping activation barriers for the s-phase are in excellent agreement with the experimental values obtained for o-LISO (255 meV from EIS, 57−74 meV from ssNMR), suggesting that the fast Li-ion conduction in o-LISO is dominated by ion transport through the s-phase. Therefore, Li-ion conduction pathways in o-LISO are thought to be primarily through the bulk of the s-phase, with additional pathways through o-DRX to interconnect the s-phase domains, as shown in Supplementary Fig. 16.

The Li-ion density averaged over the AIMD trajectories is visualized in Figs. 5c-d for o-DRX and s-phase. Both feature ion hopping through face-sharing Li polyhedra. In a stoichiometric rocksalt structure where all cations occupy Oct positions, the energy for Li-ion hopping through a Tet vacancy is high (Fig. 5e, left) unless no high-valent metal ions occupy the face-sharing sites around the tetrahedron ("0-TM"), as revealed in studies on DRX cathodes[31,32]. The over-stoichiometry in our materials requires simultaneous occupancy of face-sharing tetrahedra and octahedra, an effect that will raise the energy of any Li occupying these sites, thereby enhancing their mobility[33]. In addition, Li in a Tet site will prefer to be surrounded by only Li in its face-sharing Oct to minimize the electrostatic interaction, thereby creating the "0-TM" channels that are typical for spinel-like ordering. The combination of these effects results in much lower activation energy in o-DRX (430 meV) compared to stoichiometric DRX (552 meV for ns-LISO) (Fig. 5e).

The preference of Tet Li to form into units surrounded by four Oct Li mimics the coordination of the Tet 8a site surrounded by 16c Oct vacancies in a regular spinel. Hence, one can think of the s-phase as a spinel with 8a and 16c occupied by Li, leading to the natural stoichiometry of $Li^{8a}(Li^{16c})_2(M^{16d})_2O_4$ ($Li_3M_2O_4$). The fact that our Li over-stoichiometry does not reach this level indicates that the spinel-like ordering is incomplete. Compared to o-DRX where the face-sharing Li polyhedrons may be isolated, the s-phase has all the Tet Li (8a) in "0-TM" channels and all the face-sharing Li 3D connected. The difference in local hopping energy (Fig. 5b) between the o-DRX and s-phase confirms the importance of these 0-TM configurations for fast hopping through the Tet site. Therefore, we observe more 3D percolating ion-diffusion pathways in the s-phase than in o-DRX (Figs. 5c−d), and the ion-migration barrier in the s-phase is further lowered (Fig. 5e,

right). The high Li-ion conductivity in both o-DRX and the s-phase indicates that the face-sharing Li configurations can generally improve Li-ion mobility in *fcc*-type oxides.

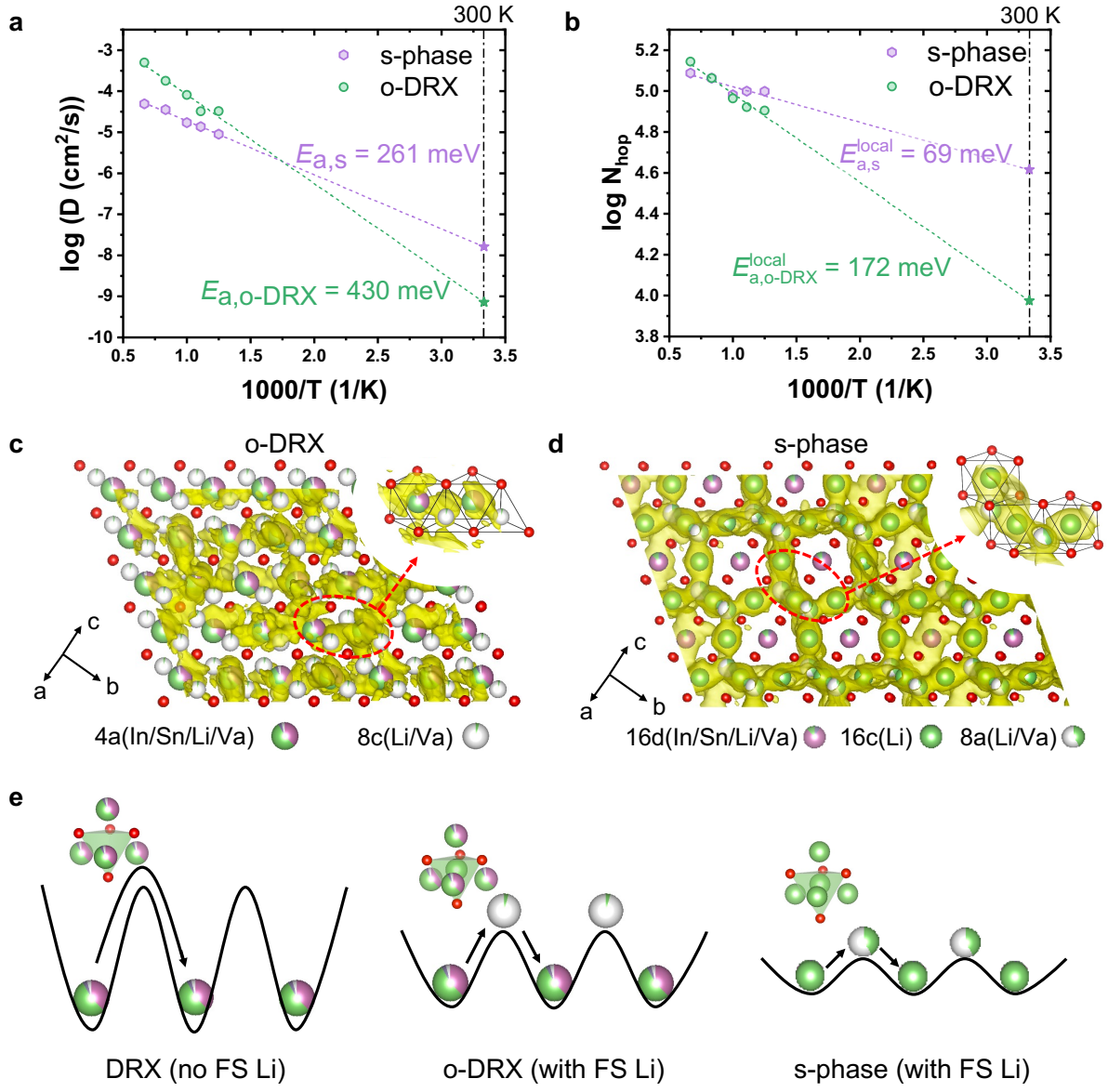

Figure 5. AIMD simulations of o-DRX and the s-phase in o-LISO. Arrhenius plots of **(a)** Li-ion diffusivities from AIMD simulations and **(b)** the number of hops between face-sharing Tet–Oct Li sites during the AIMD trajectory (80 ps) for o-DRX and the s-phase. The calculated Li-ion probability density in **(c)** o-DRX and **(d)** the s-phase from AIMD simulations at 800 K. The atomic structures are overlaid, wherein Li, In, Sn, O, and vacancies are colored green, purple, dark purple,

red, and white, respectively. **(e)** Schematic illustrations of the energy landscapes for Li-ion migration in stoichiometric DRX without face-sharing Li, o-DRX and the s-phase with face-sharing Li (left to right).

Compositional design guidelines for ORX

The success in constructing face-sharing Li configurations and the realization of high Li-ion conductivity in o-LISO motivate us to explore a broader M_1–M_2 compositional space beyond In-Sn system to create ORX-based SICs. To investigate compositions that may stabilize the presence of Li over-stoichiometry, we performed a high-throughput screening of ORX compositions via DFT calculations. We selected 16 redox-inactive metal species for making rocksalt-type $Li_{1+x+2y}M1_zM2_{1-x-z}O_2$ compositions, where y is the Li over-stoichiometry level that makes the overall cation/anion ratio larger than 1, x is the Li-excess level that leads to Li substitution of other metal cations in Oct sites while keeping the cation/anion ratio, and z can be calculated based on charge neutrality. The energy stability of each composition is evaluated by analyzing its competing phases and calculating the corresponding average energy above hull (E_{hull}) from all the considered structural configurations. More computational details can be found in the Methods section. Fig. 6a presents a metal-compatibility heatmap, where each pixel represents the average E_{hull} of computed compositions for the selected metal pairs. Darker blue color represents a lower average E_{hull}, indicating that the corresponding M_1-M_2 couple can better accommodate the face-sharing configurations created by Li over-stoichiometry. From Fig. 6a we find that using larger metal cations (e.g., In^{3+}) tends to result in greater stability, with an average E_{hull} below 80 meV/atom. In a rocksalt structure, the ionic radius of the octahedrally coordinated metal cation usually determines the volume of its face-sharing Tet vacancy[34]. Larger octahedral cations create a more

spacious Tet site for Li to reside in and thus stabilize Li over-stoichiometry. We note that La^{3+} is an exception here, as it is too large to stabilize a six-fold coordination with oxygen[35].

To further deconvolute the effect of Li content on the stability of ORX compounds, we investigate the probability distribution of E_{hull} for all the computed chemistries at the considered Li-excess (x) and Li over-stoichiometry (or Li vacancy) levels (y), as plotted in Fig. 6b. From the lower panel, we find that the probability density distribution centers at lower median E_{hull} values for compositions with Li over-stoichiometry (y = 1/12, 1/6) compared to those with Li vacancies at Oct sites (y = -1/6). This indicates that a low to intermediate Li over-stoichiometry level is easier to be incorporated into rocksalt lattice than Li vacancies. As shown in the upper panel, higher Li-excess level monotonically shifts the E_{hull} distribution downward in the given x-range, indicating that Li-excess helps to stabilize the over-stoichiometric Li present in the system. This role of Li-excess may be attributed to its electrostatic modifications on the local face-sharing environment. Specifically, more Li excess lower the average valence of the octahedral cations and introduce more occurrence of Li occupying face-sharing Oct sites around Tet Li or even "0-TM" channels, thus reducing the electrostatic repulsion felt by Tet Li[31]. Therefore, large redox-inactive metal cations (e.g., In^{3+}) and a high Li-excess level are key to stabilizing ORX compounds with face-sharing Li configurations.

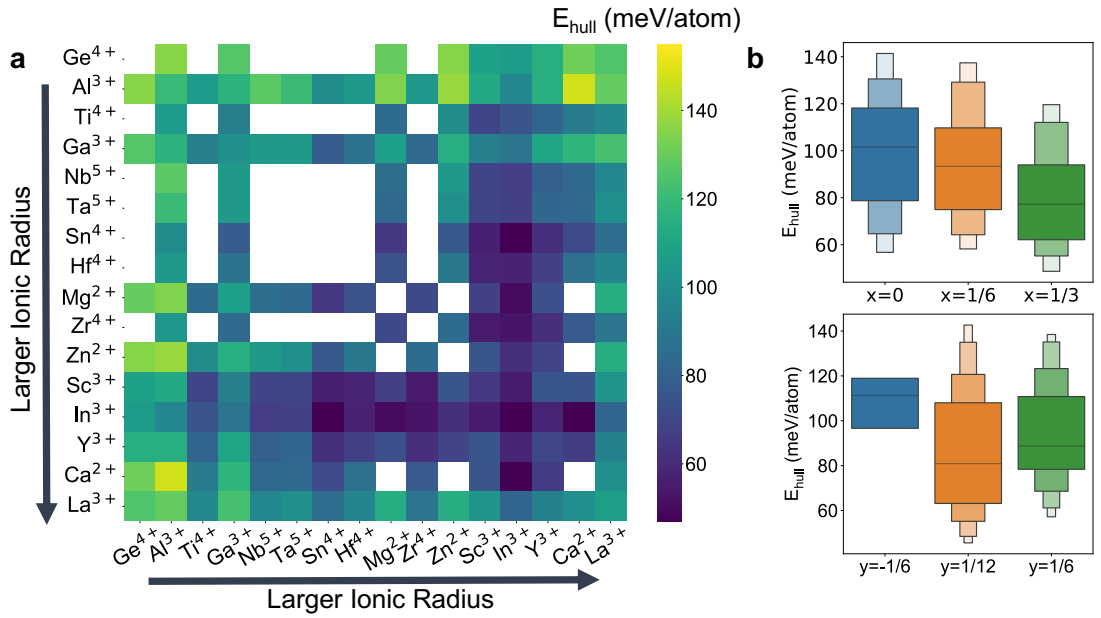

Figure 6. High-throughput computational phase-stability analysis. (a) A metal compatibility heatmap extracted from high-throughput DFT calculations. The average E_{hull} values among all the considered structural configurations for the selected binary metal chemical spaces were averaged over all computed compositions with Li-excess level x = 0, 1/6, 1/3 and Li over-stoichiometry level y = 1/12, 1/6. Darker blue indicates lower E_{hull} values and greater stability, while brighter green indicates poorer stability. **(b)** The probability density distribution of E_{hull} for all computed compounds at different Li-excess levels (x, upper panel) and Li over-stoichiometric levels (y, lower panel). A negative y indicates Li vacancy at Oct sites.

Outlook for over-stoichiometric rocksalt-type SICs

The local cation configurations play a vital role in achieving high Li-ion conductivity, especially for oxides which have weaker anion polarizability than the heavier anion chemistries such as S, Cl and Br. Despite being the most common anion packing for oxides, the *fcc* arrangement of oxygen ions has traditionally been considered unfavorable for fast ion conduction. Our strategy has been

to introduce face-sharing cations by introducing Li over-stoichiometry, giving Li higher mobility. The ordering of $Li_{Tet}(Li_{Oct})_4$ face-sharing clusters into a spinel-like arrangement provides good percolation and 3D-connectivity of the activated Li ions. The resulting ORX compound, o-LISO shown in this work, exhibits a Li-ion conductivity of 3.38×10^{-4} S cm^{-1} at ambient temperature with a low activation energy of 255 meV, which is significantly superior compared to that of *fcc*-type oxides without face-sharing Li. Considering the remarkable robustness of the rocksalt structure to chemical variation, the discovery of ORX-based SICs significantly expands the scope of potential solid-state electrolytes for ASSBs. As an extension of the In–Sn compound introduced in this work, we also experimentally prepared ORX compounds in the In–Mg, In–Zn, and In–Ti chemical spaces. All these ORX compounds show similar s-phase formation with Li over-stoichiometry and exhibit significantly improved Li-ion conductivities reaching 10^{-5}–10^{-4} S cm^{-1} at RT (Supplementary Fig. 17 and Note 6). We have further pointed out that the use of large redox-inactive metal cations and high Li-excess level are key to stabilize the face-sharing Tet Li in future ORX-type SICs design.

The observation of a spinel-like ordering in an over-stoichiometric rocksalt is at first surprising given that spinel is normally found for cation/anion ratio close to 0.75. Our finding of the new s-phase illustrates the isomorphism between the s-phase and regular spinel once one considers the equivalence between 16c vacancies in regular spinel and Li-occupied 16c in the s-phase. In a regular spinel the occupancy of the 8a Tet site forces 16c vacancies creating a “spinel unit” consisting of one 8a and four 16c sites. In the s-phase, this unit is created by the preference of a Tet Li to have four Li ions in its face-sharing Oct. The spinel is ultimately, the regular ordering of these units. This unique s-phase structure leads to a 3D fully percolated Li-ion diffusion pathway composed of 8a−16c−8a face-sharing polyhedra, resulting in a high Li-ion conductivity of 3.17×10^{-3} S cm^{-1} at 300 K in AIMD simulations. We observe that the s-phase forms as nanosized

domains in the o-DRX matrix. The co-existence of s-phase and o-DRX is thus merely a result of different cation orderings within the same continuous anion sublattice.

By cyclic voltammetry tests and interfacial chemical reaction energy calculations (Supplementary Fig. 18, Table 4, Note 7), we further evaluated that o-LISO shows great oxidative stability (up to 4 V) and excellent chemical stability with known cathodes (e.g., $LiCoO_2$, $Li(NiMnCo)_{1/3}O_2$), although its poor stability with Li metal due to easy reduction of In^{3+} needs to be further addressed by replacing In^{3+} with other more reductively stable cations or by appropriate boundary layers.

In summary, we demonstrate that incorporating excess Li to form cation over-stoichiometry in rocksalt-type lattices is an effective approach to create face-sharing Li configurations, which yields Li superionic conductivity in an *fcc*-type oxide. Such Li over-stoichiometry is achievable through straightforward solid-state synthesis and induces local spinel-like metal ordering to reduce the electrostatic repulsion between face-sharing sites. As a result, the s-phase with 3D fully connected face-sharing Li polyhedra forms as nanosized domains in the o-DRX matrix. We further show that large metal cations and substantial Li-excess are beneficial for accommodating the over-stoichiometric Li and stabilizing the face-sharing Li configurations. Our discovery provides guidelines and unlocks the potential of designing Li superionic conductors within the vast chemical space of *fcc*-type oxides.

Acknowledgements

This work was supported by the Assistant Secretary for Energy Efficiency and Renewable Energy, Vehicle Technologies Office, of the U.S. Department of Energy under Contract No. DE-AC02-05CH11231. ZL and CPG were supported by an ERC Advanced Investigator Grant for Prof. Clare Grey (EC H2020 ERC 835073). The computational analysis was performed using computational resources sponsored by the DOE's Office of Energy Efficiency and Renewable Energy and located at the National Renewable Energy Laboratory. Computational resources were also provided by the Extreme Science and Engineering Discovery Environment (XSEDE), supported by National Science Foundation grant number ACI1053575, and the National Energy Research Scientific Computing Center (NERSC), a DOE Office of Science User Facility supported by the Office of Science and the U.S. Department of Energy under Contract No. DE-AC02-05CH11231. This research also used the Lawrencium computational cluster resource provided by the IT Division at Lawrence Berkeley National Laboratory (Supported by the Director, Office of Science, Office of Basic Energy Sciences of the U.S. Department of Energy under contract no. DE-AC02-05CH11231). Work at the Molecular Foundry, LBNL was supported by the Office of Science, Office of Basic Energy Sciences of the U.S. Department of Energy under Contract No. DE-AC02-05CH11231. This work used resources at the Spallation Neutron Source, a DOE Office of Science User Facility operated by the Oak Ridge National Laboratory. This research used the mail-in program at Beamline 17-BM of the Advanced Photon Source, a U.S. Department of Energy (DOE) Office of Science User Facility, operated for the DOE Office of Science by Argonne National Laboratory under Contract No. DE-AC02-06CH11357. The TEM work was carried at the Environmental Molecular Sciences Laboratory (EMSL), a national scientific user facility

sponsored by the DOE's Office of Biological and Environmental Research and located at PNNL. PNNL is operated by Battelle for the U.S. DOE under the Contract DE-AC05- 76RL01830.

Author contributions

Y.C. planned the project with G.C., H.J., B.O.; Y.C. designed, synthesized, characterized and electrochemically tested the proposed compounds with the help from H.J., X.Y., and Z.C.; B.O. performed DFT, AIMD simulations and analyzed the data with the help from X.Z.; Z.L. acquired and analyzed the NMR data with input from C.P.G. and C.A.O.; K.P.K and L.L. acquired and analyzed TEM data with input from C.W.; Y.S. acquired and analyzed SEM data; Y.C. performed refinements of XRD and ToF-NPD data; B.O. helped with analysis of ToF-NPD data; The manuscript was written by Y.C. and revised by Z.L., X.Z., H.J., B.O., C.P.G. and G.C. with the help of all other authors. All authors contributed to discussions.

Competing interests

The authors declare no competing interests.

References:

1 Janek, J. & Zeier, W. G. A solid future for battery development. *Nature Energy* **1**, 16141, doi:10.1038/nenergy.2016.141 (2016).

2 Manthiram, A., Yu, X. & Wang, S. Lithium battery chemistries enabled by solid-state electrolytes. *Nature Reviews Materials* **2**, 16103, doi:10.1038/natrevmats.2016.103 (2017).

3 Zhang, Z. *et al.* New horizons for inorganic solid state ion conductors. *Energy & Environmental Science* **11**, 1945-1976, doi:10.1039/C8EE01053F (2018).

4 Zhao, Q., Stalin, S., Zhao, C.-Z. & Archer, L. A. Designing solid-state electrolytes for safe, energy-dense batteries. *Nature Reviews Materials* **5**, 229-252, doi:10.1038/s41578-019-0165-5 (2020).

5 Kamaya, N. *et al.* A lithium superionic conductor. *Nature Materials* **10**, 682-686, doi:10.1038/nmat3066 (2011).

6 Kato, Y. *et al.* High-power all-solid-state batteries using sulfide superionic conductors. *Nature Energy* **1**, 16030, doi:10.1038/nenergy.2016.30 (2016).

7 Zhou, L., Assoud, A., Zhang, Q., Wu, X. & Nazar, L. F. A New Family of Argyrodite Thioantimonate Lithium Superionic Conductors. *Journal of the American Chemical Society*, doi:10.1021/jacs.9b08357 (2019).

8 Richards, W. D., Miara, L. J., Wang, Y., Kim, J. C. & Ceder, G. Interface Stability in Solid-State Batteries. *Chemistry of Materials* **28**, 266-273, doi:10.1021/acs.chemmater.5b04082 (2016).

9 Xiao, Y. *et al.* Understanding interface stability in solid-state batteries. *Nature Reviews Materials*, doi:10.1038/s41578-019-0157-5 (2019).

10 Wenzel, S. *et al.* Direct Observation of the Interfacial Instability of the Fast Ionic Conductor Li10GeP2S12 at the Lithium Metal Anode. *Chemistry of Materials* **28**, 2400-2407, doi:10.1021/acs.chemmater.6b00610 (2016).

11 Muramatsu, H., Hayashi, A., Ohtomo, T., Hama, S. & Tatsumisago, M. Structural change of Li2S–P2S5 sulfide solid electrolytes in the atmosphere. *Solid State Ionics* **182**, 116-119 (2011).

12 Kim, K. J., Balaish, M., Wadaguchi, M., Kong, L. & Rupp, J. L. M. Solid‐State Li–Metal Batteries: Challenges and Horizons of Oxide and Sulfide Solid Electrolytes and Their Interfaces. *Advanced Energy Materials* **11**, 2002689, doi:10.1002/aenm.202002689 (2020).

13 Murugan, R., Thangadurai, V. & Weppner, W. Fast Lithium Ion Conduction in Garnet-Type Li7La3Zr2O12. *Angewandte Chemie International Edition* **46**, 7778-7781, doi:10.1002/anie.200701144 (2007).

14 Wang, C. *et al.* Garnet-Type Solid-State Electrolytes: Materials, Interfaces, and Batteries. *Chemical Reviews* **120**, 4257-4300, doi:10.1021/acs.chemrev.9b00427 (2020).

15 Aono, H., Sugimoto, E., Sadaoka, Y., Imanaka, N. & Adachi, G. y. Ionic conductivity of solid electrolytes based on lithium titanium phosphate. *Journal of the electrochemical society* **137**, 1023 (1990).

16 Adachi, G.-y., Imanaka, N. & Tamura, S. Ionic Conducting Lanthanide Oxides. *Chemical Reviews* **102**, 2405-2430, doi:10.1021/cr0103064 (2002).
17 Wang, Y. *et al.* Design principles for solid-state lithium superionic conductors. *Nature Materials* **14**, 1026-1031, doi:10.1038/nmat4369 (2015).
18 He, X., Zhu, Y. & Mo, Y. Origin of fast ion diffusion in super-ionic conductors. *Nature Communications* **8**, 15893, doi:10.1038/ncomms15893 (2017).
19 Chen, Y. *et al.* Solid-State Calcium-Ion Diffusion in Ca1.5Ba0.5Si5O3N6. *Chemistry of Materials* **34**, 128-139, doi:10.1021/acs.chemmater.1c02923 (2021).
20 Zhang, W. *et al.* Kinetic pathways of ionic transport in fast-charging lithium titanate. *Science* **367**, 1030, doi:10.1126/science.aax3520 (2020).
21 Liu, H. *et al.* A disordered rock salt anode for fast-charging lithium-ion batteries. *Nature* **585**, 63-67, doi:10.1038/s41586-020-2637-6 (2020).
22 Satya Kishore, M. V. V. M. *et al.* The rock salt oxide Li2MgTiO4: Type I dielectric and ionic conductor. *Materials Research Bulletin* **41**, 1378-1384, doi:https://doi.org/10.1016/j.materresbull.2005.12.003 (2006).
23 McLaren, V. L., Kirk, C. A., Poisot, M., Castellanos, M. & West, A. R. Li+ ion conductivity in rock salt-structured nickel-doped Li3NbO4. *Dalton Transactions*, 3042-3047, doi:10.1039/B316396M (2004).
24 Shiiba, H., Nakayama, M. & Nogami, M. Ionic conductivity of lithium in spinel-type Li4/3Ti5/3O4–LiMg1/2Ti3/2O4 solid-solution system. *Solid State Ionics* **181**, 994-1001, doi:https://doi.org/10.1016/j.ssi.2010.06.003 (2010).
25 Dupke, S. *et al.* Structural characterization of the lithium silicides Li15Si4, Li13Si4, and Li7Si3 using solid state NMR. *Physical Chemistry Chemical Physics* **14**, 6496-6508, doi:10.1039/C2CP24131E (2012).
26 Gao, Y. *et al.* Classical and Emerging Characterization Techniques for Investigation of Ion Transport Mechanisms in Crystalline Fast Ionic Conductors. *Chemical Reviews*, doi:10.1021/acs.chemrev.9b00747 (2020).
27 Buschmann, H. *et al.* Structure and dynamics of the fast lithium ion conductor "Li7La3Zr2O12". *Physical Chemistry Chemical Physics* **13**, 19378-19392, doi:10.1039/C1CP22108F (2011).
28 Winter, E. *et al.* 7Li NMR Studies of Short-Range and Long-Range Lithium Ion Dynamics in a Heat-Treated Lithium Iodide-Doped Lithium Thiophosphate Glass Featuring High Ion Conductivity. *The Journal of Physical Chemistry C*, doi:10.1021/acs.jpcc.0c08801 (2020).
29 Schlenker, R. *et al.* Structure and Diffusion Pathways in Li6PS5Cl Argyrodite from Neutron Diffraction, Pair-Distribution Function Analysis, and NMR. *Chemistry of Materials*, doi:10.1021/acs.chemmater.0c02418 (2020).
30 Stewner, F. & Hoppe, R. „Kationenreiche" Oxide Die Kristallstruktur von Li3InO3. *Zeitschrift für anorganische und allgemeine Chemie* **374**, 239-258, doi:https://doi.org/10.1002/zaac.19703740304 (1970).
31 Lee, J. *et al.* Unlocking the potential of cation-disordered oxides for rechargeable lithium batteries. *Science* **343**, 519-522 (2014).
32 Clément, R. J., Lun, Z. & Ceder, G. Cation-disordered rocksalt transition metal oxides and oxyfluorides for high energy lithium-ion cathodes. *Energy & Environmental Science* **13**, 345-373, doi:10.1039/C9EE02803J (2020).

33 Jun, K. *et al.* Lithium superionic conductors with corner-sharing frameworks. *Nat Mater* **21**, 924-931, doi:10.1038/s41563-022-01222-4 (2022).
34 Urban, A., Lee, J. & Ceder, G. The Configurational Space of Rocksalt-Type Oxides for High-Capacity Lithium Battery Electrodes. *Advanced Energy Materials* **4**, 1400478, doi:10.1002/aenm.201400478 (2014).
35 Waroquiers, D. *et al.* Statistical Analysis of Coordination Environments in Oxides. *Chemistry of Materials* **29**, 8346-8360, doi:10.1021/acs.chemmater.7b02766 (2017).

Methods

Synthesis: All of the Li−In−Sn−O (LISO) compounds were synthesized using a traditional solid-state method. Li_2CO_3 (Alfa Aesar, ACS, 99%min), In_2O_3 (Sigma-Aldrich, 99.998%), and SnO_2 (Sigma-Aldrich, 99.9%) were used as precursors. All the precursors were stoichiometrically mixed in ethanol (except that 10% excess Li_2CO_3 was added to compensate for the Li loss during synthesis) in a 50-mL stainless steel jar with five 10-mm-diameter stainless steel balls using a Retsch PM200 planetary ball mill at 250 rpm for 12h. The precursors were then dried overnight in a 70 °C oven and pelletized. The precursor pellets were first calcinated in air at 1050 °C and air-quenched to room temperature. After the calcination, the pellets were manually ground into powders and shaker-milled for 30 min in air using a SPEX 8000M mixer/mill to decrease the particle size. The resulting powders were pelletized and sintered in air again at 1050 °C to densify the pellets. The sintered pellets were air-quenched to room temperature and transferred to a glovebox for further study. The calcination and sintering times, respectively, were 4 and 6 h for o-LISO and 6 and 10 h for ns-LISO. The calcination and sintering times must be well controlled to ensure the appropriate amount of Li loss, and they can be dependent on the furnace because it affects the Li-loss rate. The key is to always add some excess Li precursors at the beginning and to use the heat-treatment time to control the Li loss to the desired amount. For example, for o-LISO, we want to achieve the Li content at which the DRX and s-phase appear without the Li_3InO_3-like phase.

Conductivity measurements: The Li-ion conductivities were evaluated using EIS with indium metal as the ion-blocking electrodes at temperatures ranging from 0 °C to 120 °C. The sintered pellets (at ~90%−95% relative density, Supplementary Fig. 15 for SEM cross-sectional images)

were first polished with sandpaper to remove the surface layer that had severe Li loss and then sandwiched between two indium films. The pellets with indium films were pressed using cold isostatic pressing (MTI, YLJ-CIP-20B) to ensure good contacts between the indium films and the pellet and then transferred into Bio-Logic Leak-tight sample holders (CESH) for the EIS measurements. The EIS measurements were performed using an EC-Lab Electrochemistry, VMP300 (Bio-Logic) in the frequency range of 7 MHz to 100 mHz with a 10-mV voltage amplitude. A Bio-Logic intermediate temperature system was used to control the temperature of the sample holder. EIS data fitting was performed using the ZView software package. The electronic conductivity was evaluated using a d.c. polarization test with indium metal as electrodes.

Electrochemistry: For cyclic voltammetry tests, a Li/liquid electrolyte/o-LISO-C cell was assembled. To make o-LISO-C films, as-synthesized o-LISO, carbon nanofibers, and polyvinylidene fluoride were mixed and dispensed in n-methyl-2-pyrrolidone (NMP) with a weight ratio of 7:2:1 to make the electrode slurry. The electrodes were prepared by casting the electrode slurry onto aluminum foils and dried in a 70 °C vacuum oven overnight. 6 mm-diameter disks with the loading of o-LISO about 2 mg were punched from the electrode films and assembled into a liquid coin cell by using Li metal foil as the counter electrode and commercial 1 M $LiPF_6$ in ethylene carbonate (EC) and dimethyl carbonate (DMC) solution (1:1 volume ratio) as the electrolyte. The cyclic voltammetry measurements were performed with a scan rate of 0.1 mV/s by using VMP300 (Bio-Logic).

Characterization: The lab XRD patterns of the as-synthesized compounds were obtained using a Rigaku MiniFlex 600 diffractometer equipped with a Cu source. The synchrotron XRD pattern of

o-LISO was obtained at Beamline 17-BM at Argonne National Lab. Time-of-flight neutron powder diffraction experiment of o-LISO was performed at the Spallation Neutron Source at Oak Ridge National Laboratory on the Nanoscale Ordered Materials Diffractometer (NOMAD)[36]. Rietveld refinement[37] was performed using the GSAS-II software package[38] and a high-throughput grid-search method (the details are described in Supplementary Fig. 11 and Note 5). Elemental analyses were performed by Galbraith Laboratories, Inc. using inductively coupled plasma optical emission spectroscopy for the Li, In, and Sn species. Scanning electron microscopy (SEM) images were collected using a Zeiss Gemini Ultra-55 analytical field-emission scanning electron microscope at the Molecular Foundry at Lawrence Berkeley National Lab (LBNL). Thermogravimetric analysis (TGA) was performed using a Q600 SDT instrument under O_2 flow.

ssNMR spectroscopy: Room-temperature and variable temperature ssNMR data on o-LISO and ns-LISO powders were acquired using a Bruker Avance IIIHD 700 MHz (16.4 T) NMR spectrometer with a Larmor frequency of 103.03 MHz for ^{6}Li. ^{6}Li spin echo room temperature spectra for o-LISO and ns-LISO were acquired using a 90° radiofrequency (RF) pulse of 3.75 μs and a 180° RF pulse of 7.5 μs at 50 W using 50-kHz magic-angle spinning (MAS) and a 1.3-mm double-resonance HX probe. A recycle delay of 5 s was used. Variable temperature ^{6}Li ssNMR data were acquired for o-LISO at 12.5-kHz MAS using a 4-mm triple-resonance HXY probe. ^{6}Li spin echo spectra were acquired using a 90° RF pulse of 6.2 μs and a 180° RF pulse of 12.4 μs at 300 W. Spin-lattice (T_1) relaxation time constants were measured using a saturation recovery experiment and spin-spin (T_2) relaxation time constants were measured using a variable-delay Hahn echo experiment. The temperature was calibrated using the ^{79}Br chemical shift of KBr. The

spectra were referenced against ^{6}Li-enriched Li_2CO_3 ($\delta(^{6}Li) = 0$ ppm). Spectra deconvolution was performed using the DMFIT software package[39].

TEM characterization: TEM samples of o-LISO and ns-LISO were prepared by dispersing the particles onto TEM lacey carbon grids inside an Ar-filled glovebox. Diffraction contrast imaging and EDS were conducted on a monochromated aberration-corrected Titan 80-300^{TM} scanning/transmission electron microscope operated at 300 kV. To obtain the dark-field diffraction contrast images, the objective aperture was inserted in the back focal plane to select the electrons scattered only from $(2\bar{2}0)_s$ planes. EDS data were collected using a Super-X detector inside a Themis Z STEM operated at 300 kV. The EDS data analysis was performed using the software "Velox", where the overlapped peaks were deconvoluted by using the stored standard reference spectra and employing a Filtered Least Squares (FLS) method to fit the peaks and remove the background.

DFT calculations: First-principles total energy calculations were performed with the Vienna ab initio simulation package (VASP) with a plane-wave basis set[40]. Projector augmented-wave potentials[41] with a kinetic energy cutoff of 520 eV and the exchange-correlation form in the Perdew–Burke–Ernzerhof generalized gradient approximation (GGA-PBE[41]) were employed in all the structural optimizations and total-energy calculations. For all the calculations, a reciprocal space discretization of 25 k-points per $Å^{-1}$ was applied, and the convergence criteria were set as 10^{-6} eV for electronic iterations and 0.02 eV/Å for ionic iterations.

For the high-throughput phase-diagram calculations, ORX compositions with Li-excess levels of x = 1/3, 1/6, or 0 and Li over-stoichiometric levels of y = 1/6 or 1/12 and compositions with 1/3

Li-excess and 1/6 intrinsic Li vacancy (y = −1/6) were considered. 16 metal cations that are redox-inactive and commonly used in solid-state electrolytes were selected, e.g., Mg^{2+}, Zn^{2+}, Ca^{2+}, Al^{3+}, Ga^{3+}, In^{3+}, Sc^{3+}, Y^{3+}, La^{3+}, Ge^{4+}, Ti^{4+}, Sn^{4+}, Zr^{4+}, Hf^{4+}, Ta^{5+}, Nb^{5+}. For each chemical composition, four different orderings, including γ-$LiFeO_2$ ordering, spinel-like ordering, layered-like ordering, and electrostatic ground state, were considered. For each type of ordering, we enumerated 10 configurations that have near-ground-state electrostatic Ewald energy for DFT calculation. The thermodynamic stability of all the ORX compositions was evaluated by constructing the convex hull of the DFT total energy for all phases in the relevant chemical space available in an internal database that contains phases from the Inorganic Crystal Structure Database (ICSD) and some compounds generated using data-mined substitution rules[42]. The convex hull ensures that each ground state has an energy lower than any linear combination of phases that leads to the same composition as the ground state. The phase stability for phases not on the hull was quantified by their energy above the hull (E_{hull}), which indicates the compound's driving force for decomposition into other ground states. E_{hull} serves as a reasonable indicator of synthetic accessibility, as experimentally accessible materials must generally have a low E_{hull}[43,44].

The interfacial chemical reaction energy was calculated based on the methodology by Richards et al[8]. For two crystalline reactants, A and B, there exists a number of possible reactions that consume arbitrary compositions of either phase (c_A and c_B) to form lower-energy phase equilibrium products, $xc_A + (1-x)c_B \rightarrow c_{equil}$. The reaction energy ΔE_{rxn} was obtained by evaluating the mixing ratio x that yielded the largest reaction driving force, as shown in Equation:

$$\Delta E_{\mathrm{rxn}} = \min_{x\in[0,1]} \left\{ E_{\mathrm{pd}}[xc_{\mathrm{A}} + (1-x)c_{\mathrm{B}}] - xE[c_{\mathrm{A}}] - (1-x)E[c_{\mathrm{B}}] \right\}$$

Here, the compositions c_A and c_B are normalized by their number of atoms; the function $E_{pd}[c]$ describes the energy of the ground-state structure or phase equilibrium at composition c

determined from phase diagrams and convex hull based on computed entries in the Materials Project database[45].

AIMD simulations: Ab initio molecular dynamics (AIMD) for both o-DRX and s-phase were performed to investigate the ionic conductivity. For both o-DRX and s-phase, we created Oct site ordering reflecting a DRX and spinel-like structure (low-temperature $LiCoO_2$ structure). The occupancies of both Tet and Oct sites were then modified to reach our target composition. After the partially disordered structures were established, we performed structural enumeration and choose 10 configurations with low Ewald electrostatic energy for DFT calculations. The resulting lowest energy structure for each phase was used for AIMD simulations. All the AIMD calculations were performed in an NVT ensemble with a time step of 1 fs and using a Nose − Hoover thermostat[46] for a period of 100 ps. The diffusion barrier was calculated by Arrhenius fitting of the diffusivity at different temperatures. The activation barrier of local hopping was calculated from the Arrhenius fitting of the local hopping amounts at different temperatures. The local hopping amounts were calculated by counting the number of jumps from the octahedral site to the tetrahedral site or vice versa.

Data availability

All data supporting the findings in this study are available within this Article and its Supplementary Information. Source data are provided with this paper. Any additional relevant data are available from the corresponding authors upon request.

References

8 Richards, W. D., Miara, L. J., Wang, Y., Kim, J. C. & Ceder, G. Interface Stability in Solid-State Batteries. *Chemistry of Materials* **28**, 266-273, doi:10.1021/acs.chemmater.5b04082 (2016).

36 Neuefeind, J., Feygenson, M., Carruth, J., Hoffmann, R. & Chipley, K. K. The nanoscale ordered materials diffractometer NOMAD at the spallation neutron source SNS. *Nuclear Instruments and Methods in Physics Research Section B: Beam Interactions with Materials and Atoms* **287**, 68-75 (2012).

37 Rietveld, H. M. A profile refinement method for nuclear and magnetic structures. *Journal of applied Crystallography* **2**, 65-71 (1969).

38 Toby, B. H. & Von Dreele, R. B. GSAS-II: the genesis of a modern open-source all purpose crystallography software package. *Journal of Applied Crystallography* **46**, 544-549 (2013).

39 Massiot, D. *et al.* Modelling one- and two-dimensional solid-state NMR spectra. *Magnetic Resonance in Chemistry* **40**, 70-76, doi:https://doi.org/10.1002/mrc.984 (2002).

40 Kresse, G. & Furthmüller, J. Efficient iterative schemes for ab initio total-energy calculations using a plane-wave basis set. *Physical Review B* **54**, 11169-11186, doi:10.1103/PhysRevB.54.11169 (1996).

41 Perdew, J. P., Burke, K. & Ernzerhof, M. Generalized Gradient Approximation Made Simple. *Physical Review Letters* **77**, 3865-3868, doi:10.1103/PhysRevLett.77.3865 (1996).

42 Hautier, G., Fischer, C., Ehrlacher, V., Jain, A. & Ceder, G. Data Mined Ionic Substitutions for the Discovery of New Compounds. *Inorganic Chemistry* **50**, 656-663, doi:10.1021/ic102031h (2011).

43 Sun, W. *et al.* The thermodynamic scale of inorganic crystalline metastability. *Science Advances* **2**, e1600225, doi:doi:10.1126/sciadv.1600225 (2016).

44 Ouyang, B. *et al.* Synthetic accessibility and stability rules of NASICONs. *Nature Communications* **12**, 5752, doi:10.1038/s41467-021-26006-3 (2021).

45 Jain, A. *et al.* Commentary: The Materials Project: A materials genome approach to accelerating materials innovation. *APL Materials* **1**, 011002, doi:10.1063/1.4812323 (2013).

46 Nosé, S. A unified formulation of the constant temperature molecular dynamics methods. *The Journal of Chemical Physics* **81**, 511-519, doi:10.1063/1.447334 (1984).